

RESEARCH ARTICLE

Micro-/nanostructure evolution of C/SiFeO(N,C) polymer-derived ceramic papers pyrolyzed in a reactive ammonia atmosphere

Johannes Peter¹  | Alexander Ott^{1,2}  | Ralf Riedel^{1,2}  | Emanuel Ionescu^{1,2}  | Hans-Joachim Kleebe¹ 

¹ Institute of Applied Geosciences, Technical University of Darmstadt, Darmstadt, Germany

² Institute of Materials Science, Technical University of Darmstadt, Darmstadt, Germany

Correspondence

Johannes Peter, Institute of Applied Geosciences, Technical University of Darmstadt, Schnittpahnstr. 9, D-64287 Darmstadt, Germany.

Email: peter@geo.tu-darmstadt.de

Funding information

Deutsche Forschungsgemeinschaft (DFG, German Research Foundation), Grant/Award Number: 411442613

Abstract

SiFeO(N,C)-based ceramic papers were prepared via a one-pot synthesis approach by dip-coating a cellulose-based paper template with a polymeric perhydropolysilazane precursor modified with iron(III)acetylacetonate. The pre-ceramic composites were subsequently pyrolyzed in ammonia atmosphere at 500, 700, and 1000°C, respectively, and the characteristics of the three resulting ceramic papers were comparatively investigated.

Scanning electron microscopy revealed that in each sample, the morphology of the template is successfully transferred on the ceramic system, with the cellulose-derived fibers being converted to elemental carbon encased by a SiFeO(N,C) coating. Electron transparent cross-sectional samples for transmission electron microscopy (TEM) were prepared from the ceramic papers, employing a standard ultramicrotomy slice cutting procedure, allowing for a detailed characterization of their in situ generated micro-/nanostructure as well as occurring crystalline phases.

TEM imaging and diffraction revealed that depending on pyrolysis temperature a different microstructure with a distinct phase assemblage is generated in the polymer-derived ceramic papers. Crystallization from the polymer precursor starts with the precipitation of wüstite ($\text{Fe}_{(1-x)}\text{O}$) nanoparticles at 700°C inside the ceramic coating and secondary $\epsilon\text{-Fe}_x\text{N}$ at the fiber-coating interface. Upon pyrolysis at 1000°C however, the sample primarily accommodates metallic α -iron nanocrystals that impart ferromagnetic characteristics to the ceramic paper. The results show that the template-assisted polymer-derived ceramic route is a feasible approach in the production of complex ceramic compounds with fibrous paper-like morphology. By adjusting the pyrolysis temperature, microstructure and phase composition of the ceramic paper can be conveniently tailored to the needs of its respective application.

This is an open access article under the terms of the [Creative Commons Attribution-NonCommercial-NoDerivs](https://creativecommons.org/licenses/by-nc-nd/4.0/) License, which permits use and distribution in any medium, provided the original work is properly cited, the use is non-commercial and no modifications or adaptations are made.

© 2021 The Authors. *Journal of the American Ceramic Society* published by Wiley Periodicals LLC on behalf of American Ceramic Society

KEYWORDS

nanocomposites, polymer precursor, pyrolysis, transmission electron microscopy, carbon

1 | INTRODUCTION

The thermal treatment of preceramic polymer precursors is a promising approach to the fabrication of advanced ceramic materials and thus has received increased attention in the past decades. The resulting polymer-derived ceramics (PDCs) are monophasic or undergo phase-separation leading to PDC-nanocomposites, depending on the composition and processing of the precursor.¹ Numerous PDCs have been investigated in the past years and were shown to exhibit good creep and oxidation resistance,² exceptional temperature stability,^{3,4} or interesting functional properties such as high piezoresistivity,⁵ biocompatibility,⁶ or sensing capabilities,⁷ offering promising aspects for future research and applications. One of the most compelling attributes of polymer precursors is that they can be chemically and structurally modified with, for instance, metal complexes or functional groups; accordingly, allowing to tailor the properties of the resulting ceramics to the needs of their respective application.^{2,8} The homogeneous incorporation of functional or catalytic metals via this route and their targeted precipitation as nanosized metallic or metal-compound crystallites is an attractive feature that is hardly realized by employing traditional sintering techniques. Also, by introducing filler materials, inert or sacrificial templates,⁹ or even additive manufacturing technology,¹⁰ the PDC route facilitates the production of a wide range of ceramic components such as fibrous, porous, coated, and composite materials with engineered microstructure.

Ceramic papers are a rather novel material class combining the unique paper-like morphology with the manifold properties of various ceramic material systems. Hence, some ceramic papers show excellent temperature stability, fire resistance, and insulating properties, making them predestined for use in harsh environments and as refractory materials.^{11,12} Moreover, chemical modification of such papers was shown to impart attractive mechanical¹³ and functional properties, such as electrical conductivity, sensing ability,¹⁴ or energy storage.¹⁵ Also, due to their inherently high surface area, ceramic papers can exhibit high adsorption rates and desirable filtration behavior, making them interesting for catalytic applications.¹⁶ The fabrication of ceramics with paper structure was originally achieved by using fibrous compounds, for instance, composed of silica, alumina, or zirconia, loaded with inorganic fillers. Later, preceramic papers consisting of organic compounds mixed with filler materials, which

undergo ceramization at high temperatures, were successfully employed in the production of ceramic papers.¹¹ Naturally, the tailorability of the resulting materials through designing the preceramic composite is an engaging quality of this approach to the preparation of various paper-like ceramics.^{17–20}

More recently, the demand for ceramic components with well-defined porosity or specific morphologies led to the exploration of template-assisted synthesis approaches. Carbonized organic templates such as pyrolyzed wood or cellulose were infiltrated via chemical vapor infiltration and reaction or liquid polymer precursors and treated at elevated temperatures leading to so-called biomorphous ceramics with their structure inherited from the respective template.^{21–24} Various materials based on, for instance, SiC,¹⁸ Si₃N₄, or TiC²² have been produced this way, illustrating the versatility of this approach. In 2008, a study reported on the successful production of aluminum nitride/carbon-based ceramic papers from the infiltration of regular cellulose-based filter papers by the sol-gel process and subsequent thermal treatment. The resulting material was shown to exhibit a fibrous morphology retained from the template while being composed of carbon fibers coated with AlN.²⁵

A similar approach has been applied in the synthesis of SiFeN-based ceramic papers, by infiltrating a cellulose paper template with an iron-modified perhydropolysilazane (PHPS) polymer precursor.²⁶ Here, the successful high-temperature pyrolytic conversion of infiltrated cellulose fibers toward elemental carbon, coated with a Si-based ceramic nano-composite layer containing finely dispersed Fe-based precipitates was reported. In a second tempering step in nitrogen atmosphere, the iron particles catalyze the growth of numerous ultra-long Si₃N₄ nanowires with Fe₃Si tips inside the macropores and on the surface of the ceramic paper via a vapor-liquid-solid mechanism.²⁷ This example shows the successful transfer of the paper morphology onto a ceramic system while, in addition, promising various ways of functionalization through tailoring precursor composition. However, it remained unsolved which processes protected the temperature-sensitive cellulose fibers from decomposition during pyrolysis, which synthesis conditions directly affect the microstructure and properties of the resulting ceramic, and how the presence of an organic template has an influence on the polymer-to-ceramic conversion of the precursor.

Answering these questions is paramount for establishing future applications of polymer-derived ceramic papers

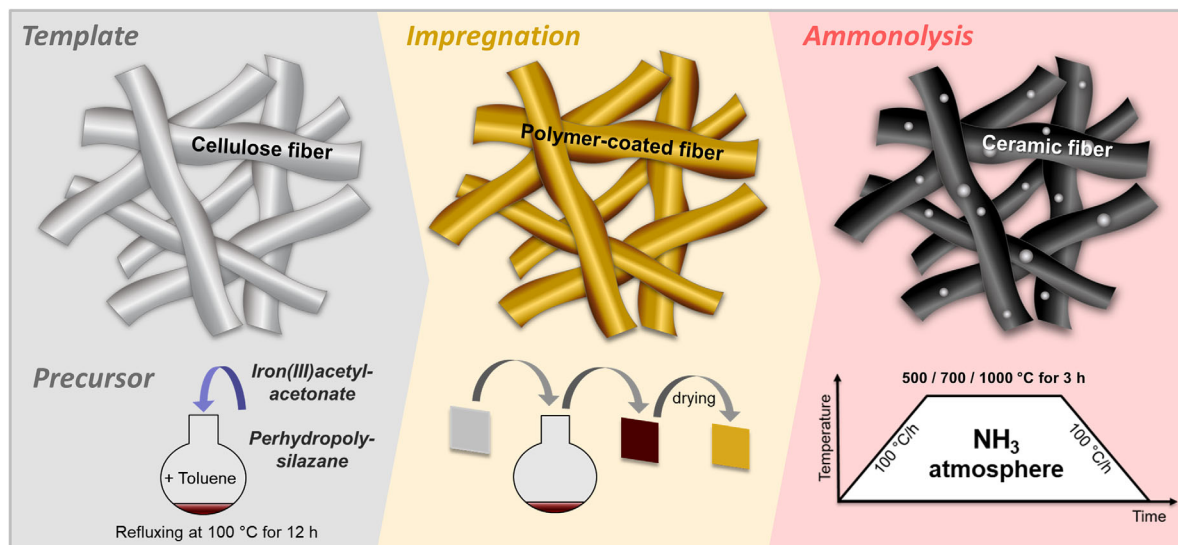


FIGURE 1 Schematic depiction of the synthesis procedure of polymer-derived ceramic papers prepared for this study. First, a PHPS-based polymer precursor is modified with iron(III)acetylacetonate by refluxing in toluene for 12 h at 100°C. Then, a cellulose-based paper template is dip-coated with the single-source precursor (SSP) solution and dried via the standard Schlenk technique. Ceramization of the preceramic composite is realized through pyrolysis in flowing ammonia atmosphere at 500, 700, and 1000°C, respectively

(PDCPs). This paper aims to fill that gap by providing a comprehensive transmission electron microscopy (TEM) investigation of ceramic paper samples with preserved microstructure prepared by employing a standard ultramicrotomy (UM) slice cutting procedure.

2 | EXPERIMENTAL PROCEDURE

The synthesis procedure of the C/SiFeO(N,C)-based ceramic papers is schematically depicted in Figure 1. First, a 20 wt.% solution of commercially available PHPS in dibutyl ether (Merck, Darmstadt, Germany) was filled into a round flask and the solvent was removed by standard Schlenk technique in an argon atmosphere. The pure PHPS was then dissolved in anhydrous toluene (99.8 %; Merck) and iron(III)acetylacetonate (Merck) was added, resulting in a liquid preceramic polymer solution, which was refluxed at 100°C for 12 h. Templates of a cellulose-based paper (Sartorius, grade: 3hw, grammage: 60 g/m²), which have been pre-cut to a size of approximately 2 cm², were dip-coated with the single-source precursor (SSP) for 1 s. Subsequently, the impregnated paper samples were vacuum dried, leading to cellulose-based preceramic papers surface modified with a SiFeN(O,C)-polymer. A reactive ammonia atmosphere was employed during pyrolysis in order to reduce the free-carbon content in the Fe(acac)₃-modified PDC coating^{28,29} as well as to increase the volume fraction of metal nitrides in the system, with the latter being considered active compounds for potential functional applications such as for exam-

ple electrocatalysis³⁰ and electromagnetic interference studies.³¹ Thermal ammonolysis was conducted in a Gero high-temperature oven (Carbolite Gero, Neuhausen, Germany) at 500, 700, and 1000°C, respectively. For each sample, the heating/cooling rate was 100 K per h and the designated peak temperature was maintained for 3 h, while a constant ammonia flow (99.999 %; Air Liquide, Paris, France) of 3 L/h during the entire ammonolysis procedure ensured minimum amounts of O₂ and H₂O in the atmosphere.

The as-synthesized inherently brittle and poorly conducting ceramic papers were mounted on conducting tape and sputtered with carbon (10 nm thick coating) for investigation via scanning electron microscopy (SEM, JEOL JSM-7600F high-resolution SEM; JEOL Company, Tokyo, Japan). SEM imaging was employed to assess their morphological characteristics and microstructure, while chemical composition information was obtained using an Oxford (Tubney Woods, Abingdon, UK) XMAX 80 EDS (energy-dispersive X-ray spectroscopy) detector.

Electron transparent cross-sectional samples for TEM investigation of the ceramic papers were prepared by employing a standard UM slice-cutting procedure. While originally used in the preparation of ultra-thin foils of biological specimen, UM-assisted sectioning has proven applicable to various inorganic materials.³² In particular, compounds with complex morphologies such as fibrous or porous ceramics are predestined for UM preparation due to the large areas of homogeneous thickness generated. Moreover, the lack of ion-thinning artifacts introduced to the sample and the possibility to generate cross-section

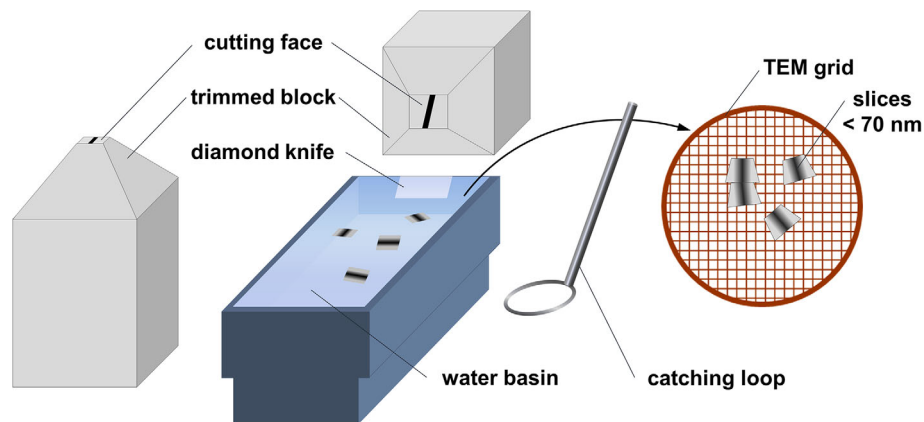


FIGURE 2 Schematic illustrating the ultramicrotomy slice cutting procedure. After embedding the ceramic paper inside an epoxy resin, the resulting sample block is trimmed to a pyramidal shape. Then, ultra-thin slices are cut from its tip by an automatically moving sample holding arm, passing a diamond knife. After each motion cycle, the forward movement is increased by a small increment to produce slices of the desired thickness. Cross-sections suitable for electron transmission (<70 nm) are determined by their interference color and transferred to a TEM sample holding grid

series that can give access to three-dimensional structure information are notable advantages.^{33,34} However, the mechanical stress applied through the diamond knife may affect the structure of the material, resulting in compressed, sheared, fractured, or textured cross-sections.³² Nevertheless, due to the otherwise high sample quality as well as its time and cost efficiency, UM can be considered a genuine alternative to classical preparation methods for electron microscopic investigation of ceramics and other inorganic materials.

For this study, the as-synthesized samples were embedded within epoxy resin sample blocks, which are trimmed to have a pyramidal shape, and subsequently, are sectioned with a Micro-Star Technologies (Bruker Corporation, Billerica, US) diamond knife (55° mounting angle; 4° clearance angle) yielding ultra-thin sample slices (50–70 nm thickness) with a trapezoidal area of approximately 150 × 200 μm. Then, the sections are transferred to a lacey carbon TEM grid and mildly coated with carbon to minimize charging from the incident electron beam. The principle of UM sample preparation is summarized in Figure 2.

The resulting cross-sectional sample slices facilitate TEM investigation of the in situ generated microstructure of the ceramic papers without the need for additional thinning steps, offering valuable insights into the structural evolution of PDCPs during pyrolysis and the corresponding cellulose-based to functional ceramic paper conversion.

Bright-field TEM (TEM-BF) and high-resolution TEM (HRTEM) images, as well as selected area electron diffraction (SAED) and nano-electron diffraction (nano-ED) patterns for micro-/nanostructural investigation, were recorded with a JEOL JEM-2100F microscope operated at 200 kV, equipped with a charge-coupled device camera and

a JEOL beryllium double tilt-holder for sample orientation, while EDS spectra were acquired using an Oxford XMAX 80 detector.

3 | RESULTS

SEM imaging in combination with chemical analyses was employed to characterize the morphological features of the ceramic papers after ammonolysis at different temperatures. Moreover, to characterize their microstructure and phase composition as well as to elucidate their temperature evolution, a combination of various TEM techniques such as BF imaging, electron diffraction, HRTEM imaging, and EDS analyses was employed.

3.1 | Ammonolysis at 500°C

In Figure 3, fiber of the sample prepared at 500°C is shown being encased by a thick ceramic coating. Wherever the evidently brittle ceramic covering is flaked off of the fiber, a distinct elemental contrast arises in the backscattered electron (BSE) image between the exposed fiber core being mainly composed of carbon (A) and the SiFeO(N,C)-based ceramic layer (B). In the higher-magnification image, the PDC coating appears homogenous, and likely phase separation has not taken place yet. Moreover, no porosity is visible in the secondary electron (SE) image, neither inside the carbon fiber nor the coating after ammonolysis at 500°C.

Figure 4 depicts a TEM-BF overview of a fiber cross-section observed in the SiFeO(N,C)-based ceramic paper prepared at 500°C. Here, the ceramic coating is still attached to the converted fiber suggesting a rather strong

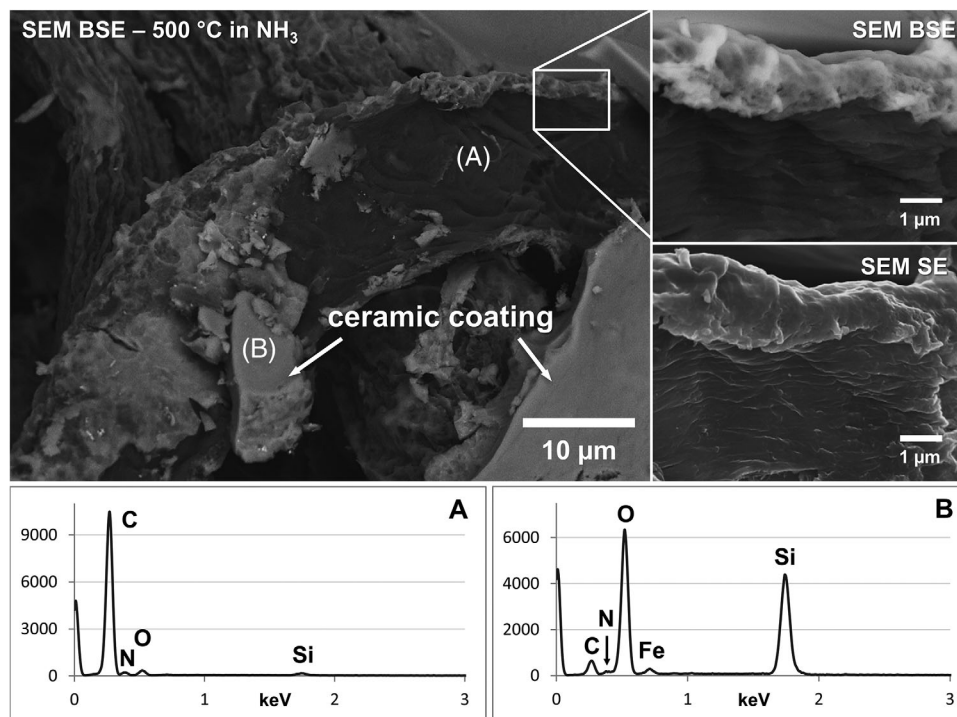


FIGURE 3 Scanning electron microscopy (SEM) backscattered electron (BSE) image of a fiber in the ceramic paper obtained upon ammonolysis at 500°C. The element contrast image allows for easy distinction between the carbon-based fiber core (A) and the SiFeO(N,C)-based ceramic coating (B), which has formed a thick layer that occasionally is flaked off of the fibers. The high-magnification inset reveals a sharp boundary between fiber and coating, while in the corresponding secondary electron (SE) image, no porosity is evident in either feature

bonding between the two components and also demonstrating the suitability of UM slice cutting for preparing such kinds of ceramic materials. Please note, however, that the ceramic layer sometimes is fragmented with individual shards overlapping. It is clear from the SEM investigation that this is an artifact from the cutting procedure that should be considered in future preparation attempts.

In this figure, the cellulose-derived fiber core (A) and the PDC coating (B) are presented along with their corresponding SAED patterns, high-magnification images, and EDS spectra. It is evident from the chemical analyses that the fiber core is almost exclusively composed of C with some minor fraction of N and O present, while the ceramic coating is SiFeO(N,C)-based, matching the SEM observations. The SAED pattern of the smooth, pore-free, and featureless fiber core displays only diffusely scattered intensity without discrete reflections relating to crystalline phases evident, while in the corresponding HRTEM image, also no signs of crystalline precipitates could be observed. This shows that the carbon fiber is entirely amorphous at temperatures of up to 500°C. However, two diffuse concentric rings are marked in both the SAED pattern and the Fast Fourier Transformation (FFT) of the HRTEM image, possibly indicating a local near-range order of the carbon atoms present; presumably, inherited by the former crys-

tallinity of the cellulose fiber or representing the very first step of graphitization of the organic fibers at elevated temperature.

The ceramic coating is characterized by its distinct mass contrast, compared to the carbon fiber it is encasing. The corresponding SAED pattern features a homogeneous Gaussian intensity distribution without signs of crystalline phases being evident. This shows that the PDC coating is still monophasic and completely amorphous at this temperature. The aforementioned fragmentation displays the brittle nature of the ceramic layer expected for a Si-based amorphous ceramic. At higher magnification, numerous pores in the range of 2–10 nm in diameter are visible throughout the coating. According to their size, the majority is classified as mesopores³⁵ being too small for observation in SEM, which rationalizes why the ceramic layer appeared smooth in the SE image. The existence of such uniform porosity strongly implies extensive gas-phase processes operating during thermal treatment of the polymeric single-source precursor (SSP) at temperatures up to 500°C. On the one hand, this could be a consequence of the release of volatile species from the cellulose fiber while, on the other hand, it certainly involves gaseous compounds emanating from the polymer precursor itself during ceramization, causing the porosity observed in this

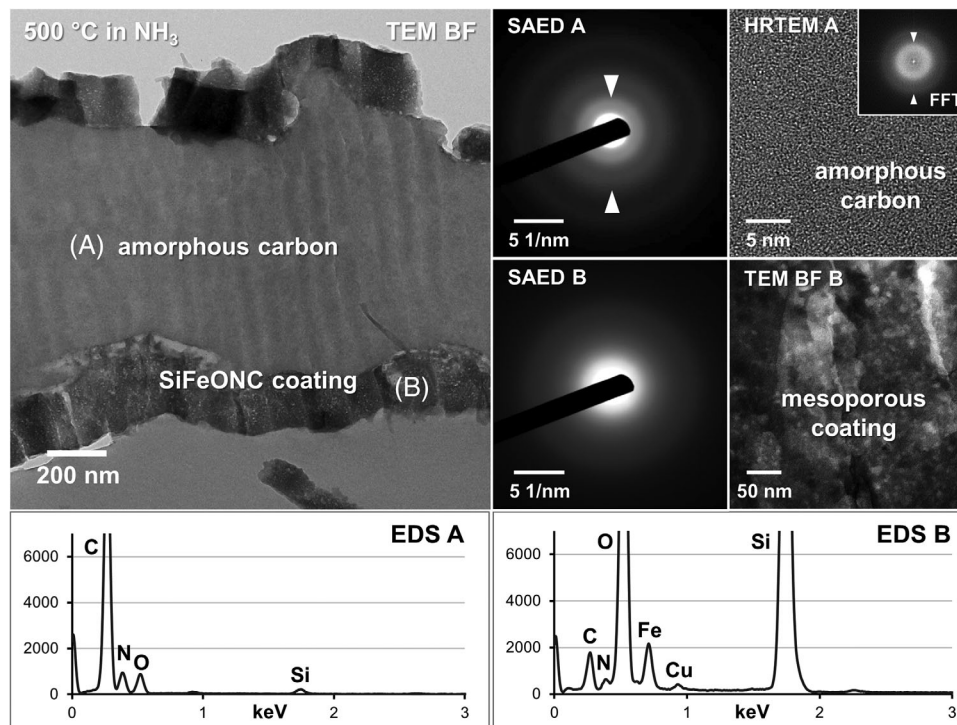


FIGURE 4 Bright-field transmission electron microscopy (TEM-BF) image of a fiber cross-section in the ceramic paper ammonolyzed at 500°C. According to the corresponding chemical analyses, sites A and B relate to the carbon fiber core (A) and the ceramic coating (B), respectively. Electron diffraction shows that the fiber core is entirely amorphous without distinct crystalline phases present, whereas the diffraction pattern and FFT of the fiber core's high-resolution TEM (HRTEM) image reveal two concentric discs that hint at a possible near-range order present in the cellulose-derived pyrolytic carbon. The ceramic coating appears highly porous in the high-magnification bright-field image, while no indications of crystalline phases are evident from the selected area electron diffraction (SAED) pattern

sample. Please note that, during TEM observation of the sample, beam damage phenomena such as sputtering and redeposition of sample atoms were observed. This suggests a still incomplete polymer-to-ceramic conversion of the precursor, while also indicating that the pyrolytic release of volatile compounds and thus the carbonization of the cellulose fiber is only partial at this rather low temperature of 500°C.

3.2 | Ammonolysis at 700°C

The structure of the ceramic paper ammonolyzed at 700°C, as observed in SEM, is depicted in Figure 5. A single fiber is shown with its core being exposed; overall, closely resembling the morphology of the sample prepared at 500°C. According to EDS analyses, the compositions of the fiber core and the coating have only changed marginally compared to the lower temperature sample, with the fiber being carbon-based and the PDC coating SiFeO(N,C)-based. The substantial carbon signal of EDS B originates in the underlying fiber indicating a small thickness of the encasing ceramic layer. Higher magnification imaging revealed some interesting differences compared to the

500°C sample. Most notably, BSE imaging shows numerous small precipitates finely dispersed over the sample surface. In addition, the SE image reveals clusters of hierarchical pores in the fiber core, whereas the coating again appears smooth without noticeable porosity.

A TEM-BF overview of a fiber cross-section in the ceramic paper obtained upon ammonolysis at 700°C is displayed in Figure 6. Again, the fiber and the ceramic coating are distinguishable by their characteristic contrast, with A being the carbonized fiber, while B represents the SiFeO(N,C)-based ceramic coating, according to their EDS spectra. The carbonized fiber appears to have undergone only minor changes compared to the 500°C ammonolyzed ceramic paper. No indications of crystalline features are visible in the SAED pattern and HRTEM image, while the EDS spectrum exhibits a slightly smaller nitrogen signal of the fiber. However, as depicted in the BF image, some pores are evident inside the fiber agreeing with the SEM observations.

Conversely, the ceramic coating (B) contains numerous precipitates that have not been observed in the lower temperature sample. The crystallites are mainly dispersed inside the amorphous ceramic matrix and give rise to discrete reflections forming a ring in the

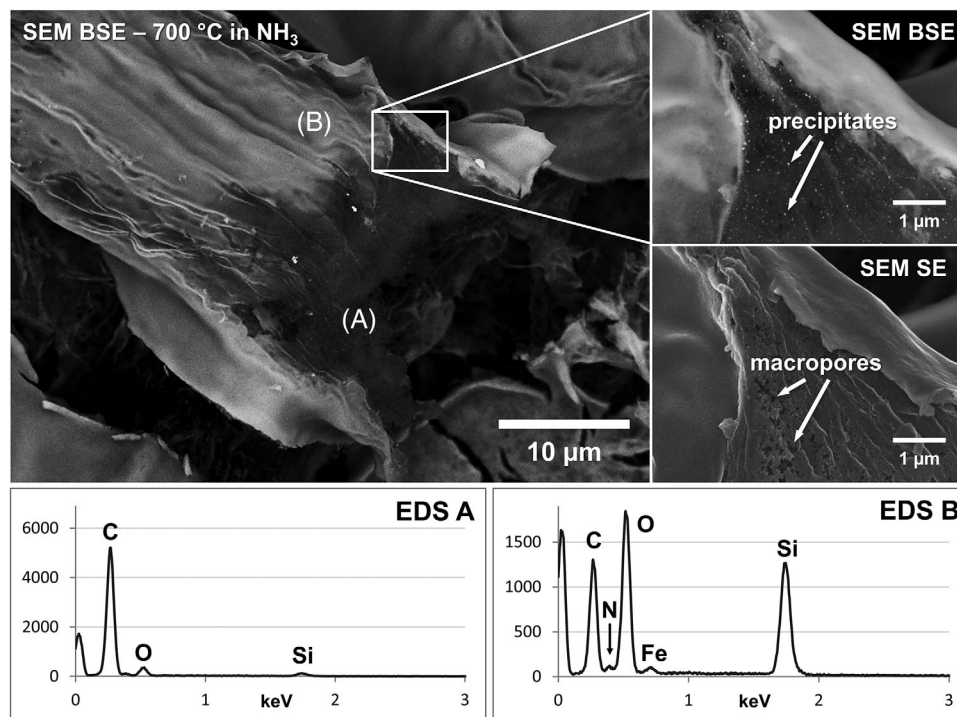


FIGURE 5 SEM-BSE image of a single fiber in the ceramic paper ammonolyzed at 700°C. Energy-dispersive X-ray spectroscopy (EDS) analyses of the fiber core (A) and a ceramic coating (B) reveal their composition to be very similar to the 500°C sample. However, the high-magnification BSE image shows small crystalline precipitates throughout the fiber, while the corresponding SE image displays numerous macropores that have formed inside the carbon fiber

SAED pattern assignable to the (2-11) lattice spacing of trigonal/hexagonal ϵ - Fe_xN , being consistent with XRD measurements conducted on this system.³⁶ The high-magnification BF image of site B shows the fiber/coating interface where two populations of precipitates exist significantly differing in size. The larger particles being located exclusively at the fiber-coating interface region range from approximately 20–50 nm, while, in addition, numerous nanosized crystallites of up to 8 nm in diameter are finely dispersed within the ceramic coating. An in-depth characterization of both populations was conducted to elucidate the phase evolution during thermal treatment of these complex ceramic composites.

Figure 7 depicts an HRTEM image of one of the larger precipitates exhibiting a prominent core-rim structure. The corresponding SAED pattern is single-crystalline and matches a low-indexed zone axis of the ϵ - Fe_xN structure. Based on the diffraction data (Figure 7B) and the EDS spectra of these larger precipitates (Figure 7C), which always accommodate a distinct nitrogen signal, it is concluded that Fe-based nitrides are one of the principal crystalline phases in the 700°C prepared sample. While the shell of the precipitate appears to be well crystallized in the HRTEM image, only very faint additional reflections occur in the diffraction pattern, which could not unequivocally be indexed as a distinct phase. However, as depicted in

the EDS spectrum, the notable carbon signal indicates the presence of an iron-carbon-based phase such as cementite Fe_3C or could resemble a phase with an intermediate composition of an iron-based carbo-nitride.

Apart from ϵ - Fe_xN , the smaller crystallites were also extensively studied to analyze their composition and structure. Figure 7D depicts an HRTEM image of a nanosized crystalline precipitate, embedded in an amorphous ceramic matrix. Nano-ED was employed to obtain structural data of individual crystallites being too minuscule for conventional selected area diffraction. The single-crystalline pattern (Figure 7E) matches iron oxide with wüstite structure ($\text{Fe}_{(1-x)}\text{O}$, $Fm-3m$), while EDS analyses of precipitate and surrounding matrix indicate that the phase is iron-based (Figure 7F). Since no significant N signal was collected and indexing of the diffraction pattern yields no solution for either α -Fe or Fe-based nitrides nor silicides, wüstite is concluded to be the nanosized phase precipitated in the PDC coating.

3.3 | Ammonolysis at 1000°C

Figure 8 depicts a fiber in the ceramic paper obtained upon ammonolysis at 1000°C. Compared to the samples prepared at lower temperatures, no clear distinction between

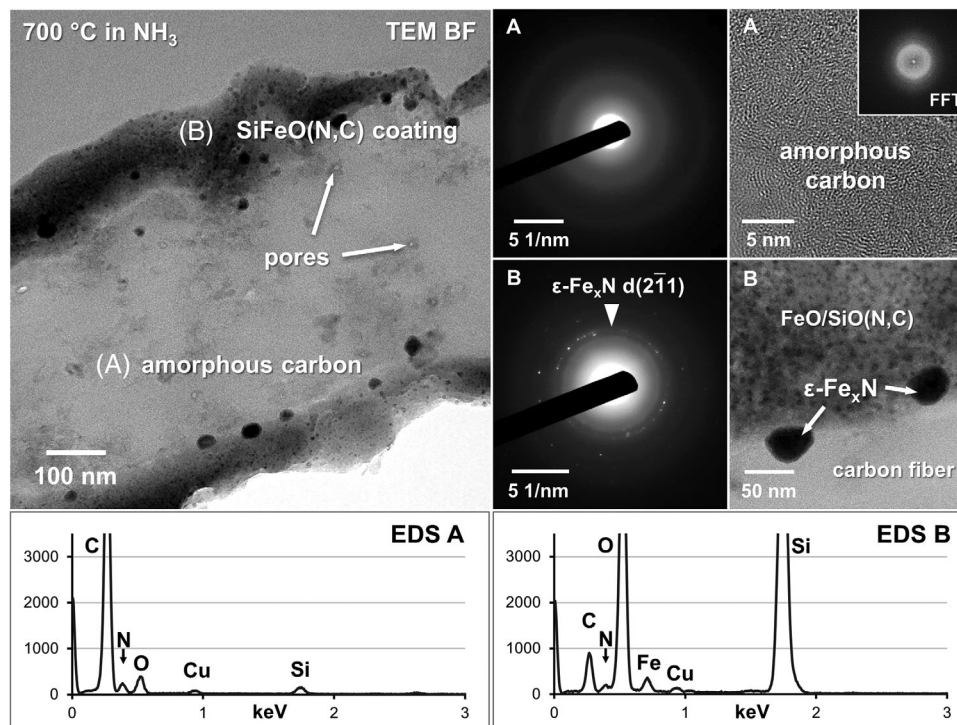


FIGURE 6 TEM-BF image of a fiber cross-section in the ceramic paper prepared at 700 °C. Again, the fiber core (A) is almost exclusively composed of amorphous carbon showing no signs of crystalline features in the corresponding SAED pattern and HRTEM image. Please note that some pores are visible inside the carbon fiber (arrows). In the SiFeO(N,C)-based ceramic coating (B), crystalline precipitates are present giving rise to discrete reflections in the SAED pattern that can be assigned to ϵ -Fe_xN. The high-magnification BF image of site B displays some of the ϵ -Fe_xN crystallites and, in addition, reveals another population of nanosized crystallites between the larger ones, being dispersed inside the SiO(N,C)-based amorphous matrix

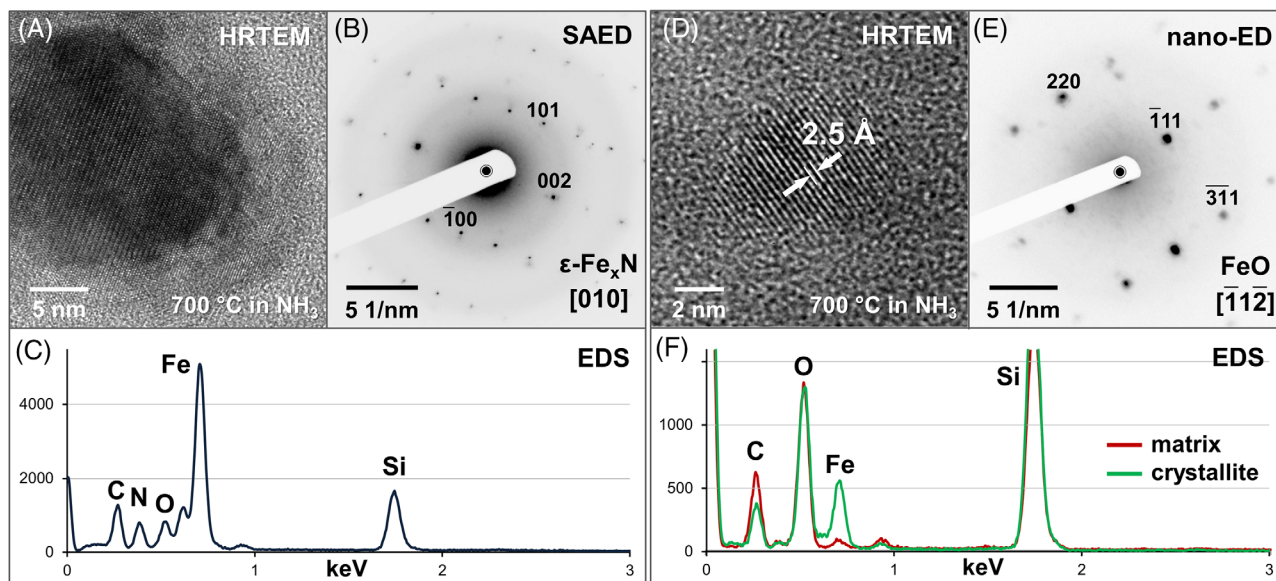


FIGURE 7 Summary of the crystalline phases observed in the 700 °C ceramic paper. Most notably, nano-sized iron-based nitrides (A) with trigonal/hexagonal structure were identified as ϵ -Fe_xN via SAED and nano electron diffraction (nano-ED) (B) in combination with EDS analyses (C). A second population of much smaller precipitates (D) dispersed inside the amorphous ceramic matrix was investigated similarly. Nano-ED (E) and comparative EDS analyses of the nanocrystals and surrounding matrix (F) show that the smaller precipitates are iron oxides that exhibit a wüstite (Fe_(1-x)O) structure

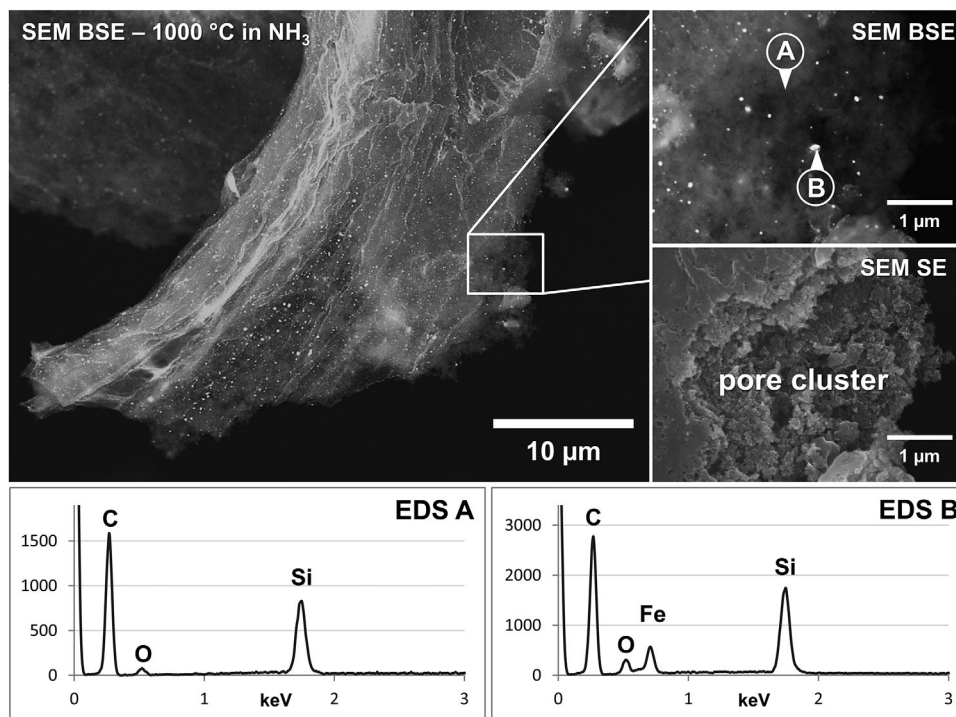


FIGURE 8 SEM-BSE image of a fiber in the 1000°C ammonolyzed ceramic paper, where no clear distinction between fiber core and coating based on elemental contrast is possible. Again, numerous precipitates are visible being much larger compared to the 700°C sample and are widely dispersed throughout the fiber. EDS analyses of and next to those features show that the precipitates contain iron while the surrounding matrix is SiOC-based. Moreover, large interconnected pores are visible in the corresponding SE image

carbon core and coating is possible based on the contrast observed in the BSE image. Again, numerous precipitates are visible throughout the fiber, which are considerably larger than in the 700°C sample and hence, noticeable even in the low-magnification SEM image. The EDS spectra show that the precipitates are iron-based, while the surrounding matrix consists mainly of carbon and silicon with an additional weak oxygen signal present. The high-magnification SE image shows large interconnected pores, which were observed throughout the sample forming hierarchical pore clusters, while other sample areas appear comparably smooth. This hints at the existence of preferential pathways for volatile species leaving the sample during pyrolysis.

In Figure 9, a TEM-BF overview of a fiber cross-section observed in the ceramic paper obtained upon ammonolysis at 1000°C is displayed. The EDS spectrum of the cellulose-derived carbon (A) closely resembles that of the samples prepared at lower temperatures; however, missing the nitrogen signal that was evident therein. Interestingly, a structural transformation of the carbon is indicated by the corresponding SAED pattern containing discrete, yet diffuse concentric rings. The innermost ring closely corresponds to the (002) lattice spacing of semicrystalline turbostratic carbon (TC), an intermediate state between amorphous carbon (AC) and graphitic carbon, representing pro-

gressing graphitization of the cellulose-derived fiber. In the HRTEM image, sets of curved lattice planes, characteristic for TC, are visible, exhibiting a lattice spacing slightly below 3.5 Å, being in close agreement with the 3.44 Å $d(002)$ spacing stated in the literature,³⁷ which however is considerably larger than that of planar graphite with 3.34 Å.³⁸ Please note that a slight intensity modulation of the TC $d(002)$ reflex ring is visible in the SAED pattern. This is a result of the TC lattice planes being preferentially oriented parallel to the fiber axis, which likely is a consequence of the original orientation of the cellulose molecular chains.

As evident from the EDS spectrum, site B corresponds to the SiFeO(C)-based PDC coating containing numerous crystalline precipitates. In the corresponding SAED pattern, a discrete reflection ring is visible, which matches the $d(110)$ spacing (2.022 Å) of metallic α -iron ($Im\bar{3}m$) implying elemental iron to be the principal crystalline phase in the sample. The HRTEM image shows several nanocrystallites exhibiting a rather uniform size distribution of 8–15 nm, dispersed inside the SiO(C)-matrix, which still is entirely amorphous upon pyrolysis at 1000°C. Figure 10A–C displays one of the nanosized precipitates with its corresponding diffraction pattern and compositional data, confirming that α -iron is the prevalent Fe-based phase inside the PDC coating. Consequently, the ceramic paper prepared at 1000°C shows ferromagnetic

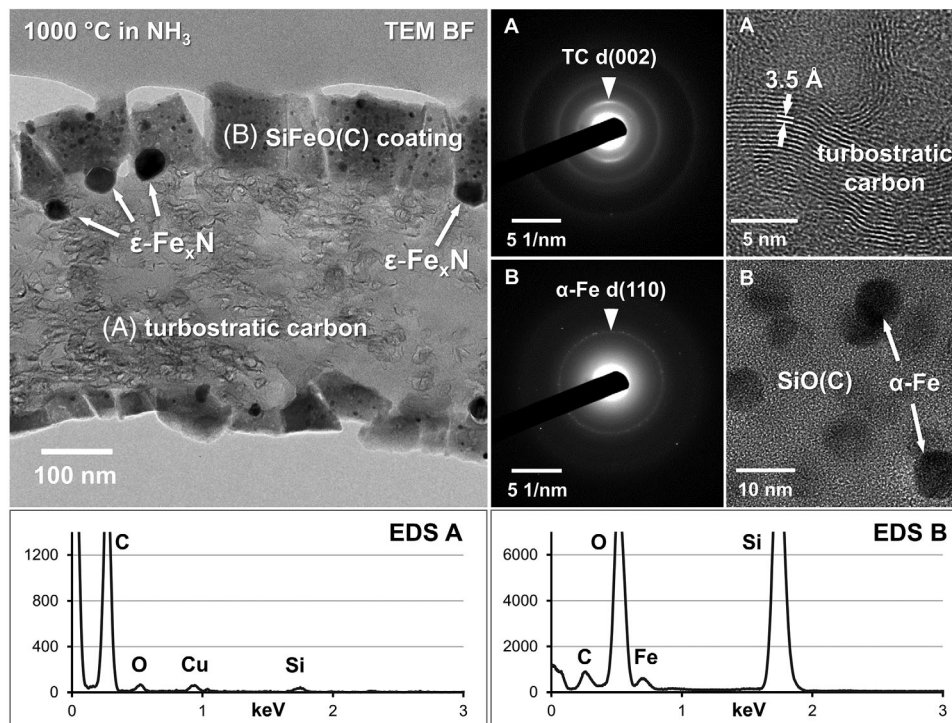


FIGURE 9 TEM-BF image of a fiber cross-section observed in the sample ammonolyzed at 1000°C. The SAED pattern of the carbon-based fiber (A) shows diffuse rings that can be attributed to the presence of turbostratic carbon with d(002) spacing of approximately 3.44 Å, exhibiting typical phase contrast of curved lattice planes in the HRTEM image. A discrete reflection ring that corresponds to the (110) spacing (2.022 Å) of α -iron is evident in the SAED pattern of the ceramic coating (B), while additional reflections are present originating from individual iron nitride particles that are typically found only at the fiber-coating interface. The HRTEM image of the coating depicts nanosized iron precipitates dispersed inside an amorphous SiO(C)-based matrix

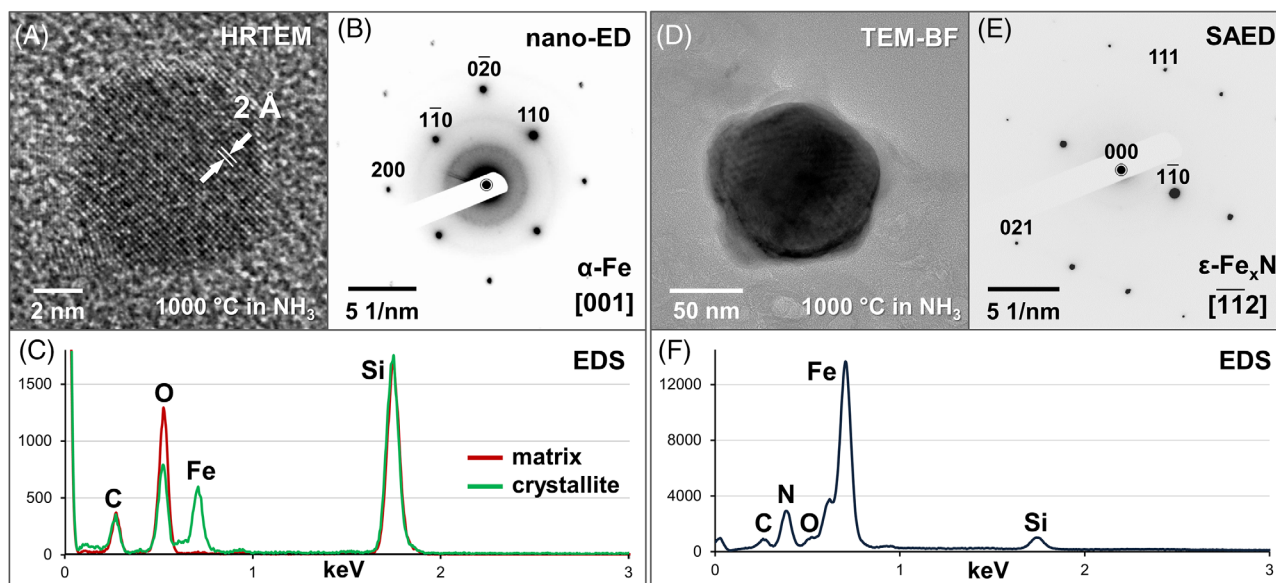


FIGURE 10 Display of the crystalline phases present in the sample prepared at 1000°C. A Fourier-filtered HRTEM image (A) of a nanosized precipitate embedded in the amorphous SiO(N,C) coating is shown along with its nano-ED pattern (B) and EDS analyses of the crystallite and the surrounding matrix (C), suggesting metallic α -iron to be the prevailing crystalline phase at this temperature. However, much larger crystallites (D) typically found at the fiber-coating interface were identified to be ϵ -Fe_xN according to electron diffraction (E) and EDS analysis (F)

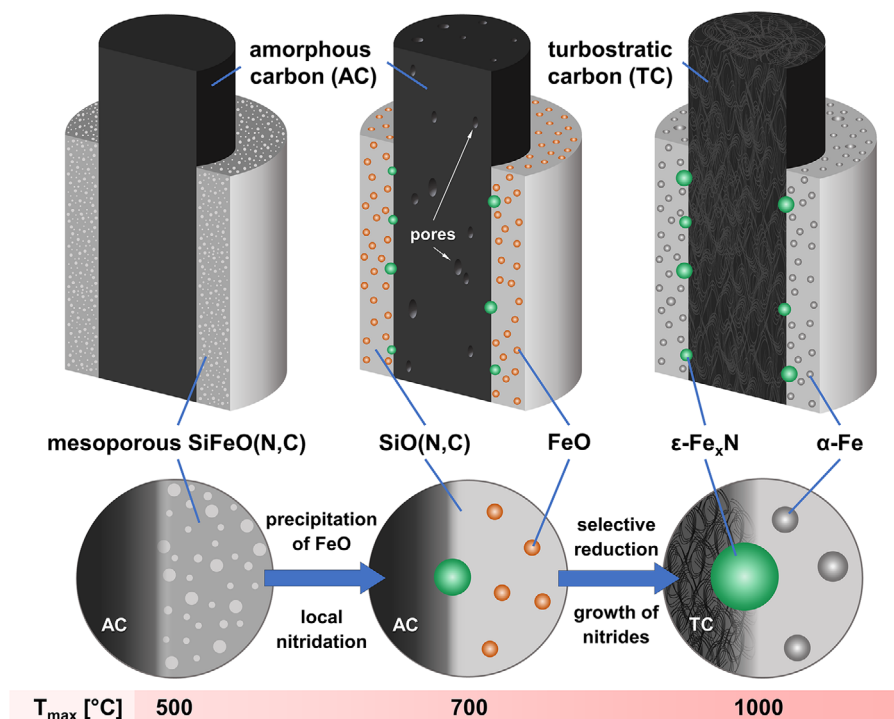


FIGURE 11 Schematic of the temperature evolution in the C/SiFeO(N,C)-based ceramic papers, showing the observed microstructure of the samples upon ammonolysis at 500, 700, and 1000°C. The proposed mechanisms leading to the phase composition of the respective temperature step are schematically depicted. For a detailed description, it is referred to the text

behavior when exposed to an external magnetic field, as opposed to the sample prepared at 700°C.

As indicated in the BF overview of Figure 9, much larger Fe-nitride particles reaching diameters of up to 100 nm, were also found typically discontinuously occurring along the fiber-coating boundary, analogous to the sample prepared at 700°C. As shown in Figure 10D–F, these particles are single-crystalline exhibiting trigonal/hexagonal ϵ -Fe_xN structure, with their composition being close to stoichiometric ϵ -Fe₃N. No nitrides were located inside the ceramic coating or the cellulose-derived carbon; a peculiarity that implies distinct chemo-physical conditions to be present at the fiber-coating interface during ammonolysis of the pre-ceramic composite.

4 | DISCUSSION

The comparative investigation of cross-sectional TEM samples prepared from SiFeO(N,C)-based PDCPs shows that very different microstructures are generated in the ceramic composites by changing the pyrolysis temperature. Figure 11 summarizes the overall findings of this study, displaying the micro-/nanostructural features observed in the samples prepared at their corresponding temperatures of 500, 700, and 1000°C.

4.1 | Polymer-derived SiFeO(N,C) coating

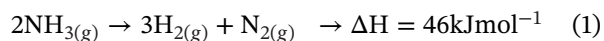
Upon ammonolysis at 500°C, the iron-modified polymer precursor is converted into a mesoporous SiFeO(N,C)-based ceramic coating. Typically, pyrolysis of PHPS in ammonia atmosphere leads to the formation of Si-N-based ceramics,³⁹ while in this case, a Si-O-based coating was generated with only subordinate N present. Without O₂ in the atmosphere, the oxygen originates from the cellulose template and from the Fe(acac)₃ used in precursor modification. The ceramic matrix is still monophasic and amorphous at this temperature and precipitation of iron-based or any other phases has not yet taken place. This suggests that the ceramization of the precursor is incomplete with its polymeric structure at least partially retained. Since it is well established that the pyrolytic reactions of PHPS take place from 100 up to 1000°C,^{39,40} the comparably low temperature and short duration of pyrolysis in this sample cause incomplete ceramization of the ceramic layer.

At an ammonolysis temperature of 700°C, countless iron oxide nanoparticles dispersed within a pore-free and amorphous SiO(N,C)-based matrix are observed. With most of them being smaller than 10 nm, and considering their homogeneous distribution, they represent the first precipitation step of iron phases from the Fe(acac)₃-modified PHPS precursor. According to TEM analysis, the

crystallites were identified as the non-stoichiometric oxide wüstite ($\text{Fe}_{(1-x)}\text{O}$), which is a metastable phase below 560°C ⁴¹ that is expected to be either oxidized toward magnetite or reduced to metallic iron, depending on the thermodynamic conditions. At 700°C , the existence of $\text{Fe}_{(1-x)}\text{O}$, without substantial magnetite or α -iron present, requires a narrow window of the oxygen content of about 23–24 wt.%, according to the Fe-O phase diagram.⁴¹ Upon cooling below 560°C , wüstite decomposes to form α -iron and magnetite for a wide compositional range. Below 300°C , however, the decomposition of wüstite is considered immeasurably slow,⁴¹ suggesting that the comparably fast cooling of the sample preserved the metastable wüstite.

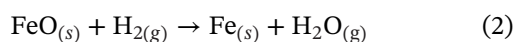
No wüstite precipitates were identified in the 1000°C sample with α -iron now being the prevalent crystalline Fe-phase. Iron particles occurred homogeneously dispersed within the otherwise amorphous and pore-free $\text{SiO}(\text{N,C})$ -based coating, implying an in situ formation directly through the local reduction of the nanosized wüstite particles. Unfortunately, many processes that lead to the reduction of the FeO precipitates are conceivable and thus, the exact mechanism cannot be determined. Several potential reducing agents exist in the system, with carbon and its monoxide being abundant in presence of the cellulose template during pyrolysis, especially, since the Boudouard equilibrium is changed at temperatures above $\approx 700^\circ\text{C}$ favoring CO formation.⁴² Moreover, generating CO consumes available oxygen, thus lowering $p\text{O}_2$ and shifting the composition in the Fe-O system toward the α -iron + wüstite two-phase field at 700°C .⁴¹

Another possible reducing agent in the crucible atmosphere is molecular hydrogen originating in the thermal decomposition of ammonia.⁴³



While this reaction is more favorable at a higher temperature,⁴⁴ the employment of a flowing ammonia atmosphere could considerably mitigate the effects of hydrogen accumulation in the atmosphere. Still, elevated H_2 concentrations may be present inside the macropores in between the fibers, potentially acting as a local reducing agent that, in addition, features comparably high diffusion rates in most materials.⁴⁵ Also, the reduction of iron oxides in both H_2 and CO atmospheres is considerably promoted with increasing temperature.

For instance, it was shown that at moderate H_2 concentrations of 10 vol.%, a temperature increase from 600 to 800°C considerably decreases the ΔG of the reaction⁴⁶ from $+1 \text{ kcal mol}^{-1}$ to $-0.3 \text{ kcal mol}^{-1}$.



4.2 | Cellulose-derived carbon fiber

The pyrolytic decomposition of cellulose has been extensively studied in the past and the processes that lead to its gradual carbonization at elevated temperatures can be divided into four successive steps: (i) loss of adsorbed water, (ii) removal of structural water, (iii) depolymerization, and (iv) aromatization or graphitization.⁴⁷

In the sample prepared at 500°C , the cellulose fiber has been converted to a large extent into amorphous elemental carbon as is evident by the low oxygen signal collected. However, the observation of electron-beam damage of the sample during TEM investigation with associated redeposition of hydrocarbons indicates pyrolytic release of volatile species from the cellulose fiber and thus, its imperfect carbonization. The maximum carbon yield of pyrolytic cellulose is close to 44.4 wt.% derived from its stoichiometry; however, due to depolymerization and carbon removal through oxygen from the cellulose itself, this is reduced to only 10–30 wt.%.⁴⁸ However, in the case of PDCPs, it is reasonable to assume that the polymeric coating inhibits the degassing of CO , CO_2 , and other carbon-based volatile compounds from the cellulose fiber, significantly decreasing the mass loss of the cellulose fibers.

In the 700°C samples, SEM and TEM imaging revealed some pores inside the fibers, potentially acting as preferential pathways for gases during pyrolysis. While the carbon was found to be still entirely amorphous, no beam damage effects were observed suggesting a rather advanced stage of carbonization.

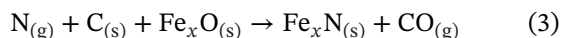
In the ceramic paper prepared at 1000°C , the cellulose fibers have now to a large extent been converted to porous TC indicating progressing graphitization. At this temperature, elemental carbon is expected to be the main component of the fiber, with only subordinate oxygen present. The lattice planes of the semi-crystalline carbon are preferentially aligned along with the fiber axis, as is evident from the intensity modulation in the electron diffraction pattern. Most likely, this results from the original cellulose fiber structure being an assemblage of nanofibril molecule chains running parallel to each other. It is shown that for different cellulose precursor structures, different microstructures and crystallinities are generated inside the corresponding cellulose-derived carbon when exposed to elevated temperatures. In particular, graphitization of cellulose fiber bundles was shown to result in an intensity modulation of the graphite $d(002)$ ring,⁴⁹ similar to that observed in this study. Therefore, the structure of the cellulose directly affects the properties of the resulting carbon-based fiber, which has to be considered when employed as a template in the production of functional PDCPs.

4.3 | Fiber-coating interface

With hexagonal ϵ -Fe_xN, another iron-based compound was found to be present within the 700 and 1000°C prepared ceramic papers, occurring exclusively at the fiber-coating interface. While it is not surprising to have metal nitrides in a sample prepared in a hot ammonia atmosphere,⁵⁰ the fact that these precipitates only exist along the contact zone of the cellulose-derived carbon and PDC coating hints at distinct chemo-physical processes operating at the boundary.

In contrast to the dense ceramic coating, the highly porous structure of pyrolytic carbon facilitates diffusion along the free volume of the fiber.⁵¹ With progressing pyrolysis, a substantial increase in meso- and microporosity is observed, enabling potentially high diffusion rates of gaseous species inside the carbon fiber. Moreover, carbon-based membranes were shown to have gas separation properties^{51,52} favoring permeation of smaller species such as H₂ (kinetic radius: 289 pm),⁵³ ammonia (260 pm),⁵⁴ and water (265 pm)⁵³ from gas mixtures containing larger species such as CO₂ (330 pm)⁵³ or N₂ (364 pm).⁵³

In consequence, diffusive NH₃ transport is expected to occur inside the fibers and along with the fiber-coating interface. Ammonia diffusing through the carbon fiber readily reacts with iron oxide precipitates along with the contact to the ceramic layer to either directly form Fe-based nitrides⁵⁵ or, if carbon is present, carbothermal reduction nitridation takes place.⁵⁶



Conversely, fast permeation through the ceramic layer is limited, rationalizing the absence of nitrides inside the coating.

At 1000°C, the ϵ -Fe_xN precipitates have not only withstood reduction but also undergone considerable growth compared to the sample prepared at 700°C, while FeO enclosed in the ceramic layer has been reduced to α -iron by either CO or H₂. According to Equation (1), ammonia decomposes due to both elevated temperature^{43,44} and catalytic conversion at ϵ -Fe_xN sites,⁵⁵ likely generating H₂ and N₂ inside the fiber. Hydrogen diffuses through the fiber, whereas N₂ is retained presumably resulting in a locally increased nitriding potential. Therefore, the proposed conditions exclusively present at the fiber-coating interface enable hexagonal ϵ -Fe_xN to be stable even at temperatures of up to 1000°C instead of being converted to cubic γ -Fe₄N or metallic α -iron.

5 | CONCLUSIONS

The present work provides insights into the micro- and nanostructural characteristics and temperature evolution

of PDCPs prepared by a one-pot synthesis approach. Cellulose-based paper templates dipped with an iron-modified PHPS-based single-source precursor were pyrolyzed in an ammonia atmosphere, yielding paper-like ceramic composites consisting of carbon fibers with a SiFeO(N,C)-based coating.

Electron microscopic investigation revealed that upon ammonolysis of the polymer-modified templates at 500°C, the cellulose fibers are converted to amorphous carbon (AC) encased by a monophasic and amorphous SiFeO(N,C)-based coating, while in the paper pyrolyzed at 700°C precipitation of wüstite nanocrystallites from the ceramic layer has taken place. At 1000°C, the oxide particles have been reduced to metallic α -iron and a structural transformation of the AC toward semicrystalline turbostratic carbon is observed, resulting in a ceramic paper with a notably distinct phase assemblage and microstructure. Moreover, at both 700 and 1000°C, ϵ -Fe_xN particles were found to exclusively occur at the fiber/coating interface, implying a higher nitriding potential inside the carbon fiber compared to the ceramic layer, which in turn is attributed to selective diffusivities of nitriding species along the free volume of the porous carbon fibers.

It was shown that the phase composition and microstructure of the PDCPs are significantly influenced by the pyrolysis temperature, offering extended pathways for the production of highly designable ceramic composites. However, employing cellulose as a template for PDCPs gives rise to complex interactions with the precursor and atmosphere during thermal treatment, which can directly affect the properties of the resulting ceramic and thus, has to be considered in future functionalization attempts.

ACKNOWLEDGMENT


Johannes Peter, Alexander Ott, Ralf Riedel, Emanuel Ionescu, and Hans-Joachim Kleebe greatly acknowledge the funding of this project by the Deutsche Forschungsgemeinschaft (DFG, German Research Foundation) under the contract number 411442613.

ORCID

Johannes Peter  <https://orcid.org/0000-0002-8760-547X>

Alexander Ott  <https://orcid.org/0000-0002-5851-2805>

Ralf Riedel  <https://orcid.org/0000-0001-6888-7208>

Emanuel Ionescu  <https://orcid.org/0000-0002-3266-3031>

Hans-Joachim Kleebe  <https://orcid.org/0000-0001-8850-1771>

REFERENCES

- Ionescu E, Kleebe H-J, Riedel R. Silicon-containing polymer-derived ceramic nanocomposites (PDC-NCs): preparative

- approaches and properties. *Chem Soc Rev.* 2012;41(15):5032. <https://doi.org/10.1039/c2cs15319j>
- Riedel R, Mera G, Hauser R, Kloneczynski A. Silicon-based polymer-derived ceramics: synthesis properties and applications—a review: dedicated to Prof. Dr. Fritz Aldinger on the occasion of his 65th birthday. *Nippon Seramikkusu Kyokai Gakujutsu Ronbunshi.* 2006;114(1330):425–44. <https://doi.org/10.2109/jcersj.114.425>
 - Wang Z-C, Aldinger F, Riedel R. Novel silicon-boron-carbon-nitrogen materials thermally stable up to 2200°C. *J Am Ceram Soc.* 2004;84(10):2179–83. <https://doi.org/10.1111/j.1151-2916.2001.tb00984.x>
 - Feng B, Peter J, Fasel C, Wen Q, Zhang Y, Kleebe H-J, et al. High-temperature phase and microstructure evolution of polymer-derived sizzrcn and sizzrbcn ceramic nanocomposites. *J Am Ceram Soc.* 2020;103(12):7001–13. <https://doi.org/10.1111/jace.17149>
 - Zhang L, Wang Y, Wei Y, Xu W, Fang D, Zhai L et al. A silicon carbonitride ceramic with anomalously high piezoresistivity. *J Am Ceram Soc.* 2008;91(4):1346–9. <https://doi.org/10.1111/j.1551-2916.2008.02275.x>
 - Fiocco L, Li S, Stevens MM, Bernardo E, Jones JR. Biocompatibility and bioactivity of porous polymer-derived Ca-Mg silicate ceramics. *Acta Biomater.* 2017;50:56–67. <https://doi.org/10.1016/j.actbio.2016.12.043>
 - Zhao R, Shao G, Cao Y, An L, Xu C. Temperature Sensor Made of polymer-derived ceramics for high-temperature applications. *Sens Actuators A.* 2014;219:58–64. <https://doi.org/10.1016/j.sna.2014.08.012>
 - Colombo P, Mera G, Riedel R, Sorarù GD. Polymer-derived ceramics: 40 years of research and innovation in advanced ceramics: polymer-derived ceramics. *J Am Ceram Soc.* 2010;93(7):1805–37. <https://doi.org/10.1111/j.1551-2916.2010.03876.x>
 - Ewert J-K, Denner C, Friedrich M, Motz G, Kempe R. Mesosstructuring of sicn ceramics by polystyrene templates. *Nanomaterials* 2015;5(2):425–35. <https://doi.org/10.3390/nano5020425>
 - Wang X, Schmidt F, Hanaor D, Kamm PH, Li S, Gurlò A. Additive manufacturing of ceramics from preceramic polymers: a versatile stereolithographic approach assisted by thiol-ene click chemistry. *Additive Manufact.* 2019;27:80–90. <https://doi.org/10.1016/j.addma.2019.02.012>
 - Travitzky N, Windsheimer H, Fey T, Greil P. Preceramic paper-derived ceramics. *J Am Ceram Soc.* 2008, 91(11), 3477–92. <https://doi.org/10.1111/j.1551-2916.2008.02752.x>
 - Koga H, Ishihara H, Kitaoka T, Tomoda A, Suzuki R, Warishi H. NO_x reduction over paper-structured fiber composites impregnated with Pt/Al₂O₃ catalyst for exhaust gas purification. *J Mater Sci.* 2010, 45(15), 4151–7. <https://doi.org/10.1007/s10853-010-4504-6>
 - Lu B-Q, Zhu Y-J, Chen F. Highly flexible and nonflammable inorganic hydroxyapatite paper. *Chem Eur J.* 2014, 20(5), 1242–6. <https://doi.org/10.1002/chem.201304439>
 - Li G, Ma J, Peng G, Chen W, Chu Z, Li Y, et al. Room-temperature humidity-sensing performance of SiC nanopaper. *ACS Appl Mater Interfaces.* 2014, 6(24), 22673–9. <https://doi.org/10.1021/am5067496>
 - Yang L, Cheng S, Ding Y, Zhu X, Wang ZL, Liu M. Hierarchical network architectures of carbon fiber paper supported cobalt oxide nanonet for high-capacity pseudocapacitors. *Nano Lett.* 2012, 12(1), 321–5. <https://doi.org/10.1021/nl203600x>
 - Tuler FE, Banús ED, Zanuttini MA, Miró EE, Milt VG. Ceramic papers as flexible structures for the development of novel diesel soot combustion catalysts. *Chem Eng J.* 2014, 246, 287–98. <https://doi.org/10.1016/j.cej.2014.02.083>
 - Windsheimer H, Travitzky N, Hofenauer A, Greil P. Laminated object manufacturing of preceramic-paper-derived Si⁺SiC composites. *Adv Mater.* 2007, 19(24), 4515–9. <https://doi.org/10.1002/adma.200700789>
 - Ghanem H, Alkhateeb E, Gerhard H, Popovska N. Oxidation behavior of silicon carbide based biomorphic ceramics prepared by chemical vapor infiltration and reaction technique. *Ceram Int.* 2009, 35(7), 2767–74. <https://doi.org/10.1016/j.ceramint.2009.03.025>
 - Gutbrod B, Haas D, Travitzky N, Greil P. Preceramic paper derived alumina/zirconia ceramics. *Adv Eng Mater.* 2011, 13(6), 494–501. <https://doi.org/10.1002/adem.201100017>
 - Junkes JA, Dermeik B, Gutbrod B, Hotza D, Greil P, Travitzky N. Influence of coatings on microstructure and mechanical properties of preceramic paper-derived porous alumina substrates. *J Mater Process Technol.* 2013, 213(2), 308–13. <https://doi.org/10.1016/j.jmatprotec.2012.09.005>
 - Sieber H, Hoffmann C, Kaindl H, Greil P. Biomorphic cellular ceramics. *Adv Eng Mater.* 2000, 2(3), 105–9.
 - Popovska N, Almeida-Streitwieser D, Xu C, Gerhard H, Sieber H. Kinetic analysis of the processing of porous biomorphic titanium carbide ceramics by chemical vapor infiltration. *Chem Vap Deposit.* 2005, 11(3), 153–8. <https://doi.org/10.1002/cvde.200306319>
 - Vyshnyakova K, Yushin G, Pereseltseva L, Gogotsi Y. Formation of porous SiC ceramics by pyrolysis of wood impregnated with silica. *Int J Appl Ceram Technol.* 2006, 3(6), 485–90. <https://doi.org/10.1111/j.1744-7402.2006.02103.x>
 - Kiselov VS, Yukhymchuk VO, Valakh MY, Tryus MP, Skoryk MA, Rozhin AG, et al. Biomorphous SiC ceramics prepared from cork oak as precursor. *J Phys Chem Solids.* 2016, 91, 145–51. <https://doi.org/10.1016/j.jpcs.2016.01.003>
 - Wang W, Xue T, Jin Z, Qiao G. Preparation and Characterization of morph-genetic aluminum nitride/carbon composites from filter paper. *Mater Res Bull.* 2008, 43(4), 939–45. <https://doi.org/10.1016/j.materresbull.2007.04.033>
 - Zhou C. Ternary Si-Metal-N ceramics: single-source-precursor synthesis, nanostructure and properties characterization. PhD Thesis; Department of Materials and Earth Sciences, Germany. 2017. <http://tuprints.ulb.tu-darmstadt.de/6145/>
 - Zhou C, Fasel C, Ishikawa R, Gallei M, Ikuhara Y, Lauterbach S, et al. One-pot synthesis of a C/SiFeN(O)-based ceramic paper with in-situ generated hierarchical micro/nano-morphology. *J Eur Ceram Soc.* 2017, 37(16), 5193–203. <https://doi.org/10.1016/j.jeurceramsoc.2017.03.007>
 - Mutin PH. Control of the composition and structure of silicon oxycarbide and oxynitride glasses derived from polysiloxane precursors. *J Sol-Gel Sci Technol.* 1999, 14(1), 27–38. <https://doi.org/10.1023/A:1008769913083>
 - Yive CKSN, Corriu RJP, Leclercq D, Mutin PH, Vioux A. Thermogravimetric analysis/mass spectrometry investigation of the thermal conversion of organosilicon precursors into ceramics

- under argon and ammonia. 2. Poly(Silazanes). *Chem Mater.* 1992, 4(6), 1263–71. <https://doi.org/10.1021/cm00024a028>
30. Little DJ, Edwards DO, Smith MR, Hamann TW. As precious as platinum: iron nitride for electrocatalytic oxidation of liquid ammonia. *ACS Appl Mater Interfaces.* 2017, 9(19), 16228–35. <https://doi.org/10.1021/acsami.7b02639>.
 31. Dai L, Xie S, Yu M, Ci L. Fabrication and electromagnetic properties of carbon-based iron nitride composite. *J Magn Magn Mater.* 2018, 466, 22–7. <https://doi.org/10.1016/j.jmmm.2018.06.046>.
 32. McMahon G, Malis T. Ultramicrotomy of nanocrystalline materials. *Microsc Res Tech.* 1995, 31(4), 267–74. <https://doi.org/10.1002/jemt.1070310403>
 33. Tucker DS, Jenkins EJ, Hren JJ. Sectioning spherical aluminum oxide particles for transmission electron microscopy. *J Elec Microsc Tech.* 1985, 2(1), 29–33. <https://doi.org/10.1002/jemt.1060020104>
 34. Li R, Wadsworth I, Young J, Acheson R. Preparation of ceramic fibre tem cross-sections using ultramicrotomy and ion beam thinning methods. *J Microsc.* 1996, 184(1), 62–6. <https://doi.org/10.1046/j.1365-2818.1996.1030660.x>
 35. Al-Naib UMB, editor. A brief introduction to porous ceramic. In: *Recent advances in porous ceramics.* London: InTechOpen; 2018. p. 1–10. <https://doi.org/10.5772/intechopen.74747>
 36. Ott A, Peter J, Wiehl L, Potapkin V, Kramm UI, Kleebe H-J, et al. Conversion of a polysilazane-modified cellulose-based paper into a C/SiFe(N,C)O ceramic paper via thermal ammonolysis. *Int J Appl Ceram Technol.* 2021,(in press). <https://doi.org/10.1111/ijac.13869>
 37. Dumanli AG, Windle AH. Carbon fibres from cellulosic precursors: a review. *J Mater Sci.* 2012, 47(10), 4236–50. <https://doi.org/10.1007/s10853-011-6081-8>
 38. Welz S, McNallan MJ, Gogotsi Y. Carbon structures in silicon carbide derived carbon. *J Mater Process Technol.* 2006, 179(1–3), 11–22. <https://doi.org/10.1016/j.jmatprotec.2006.03.103>
 39. Funayama O, Tashiro Y, Kamo A, Okumura M, Isoda T. Conversion mechanism of perhydropolysilazane into silicon nitride-based ceramics. *J Mater Sci.* 1994, 29(18), 4883–8. <https://doi.org/10.1007/BF00356538>
 40. Ma FL, Qi HM, Zhu YP, Ren XW, Wang F. Thermal cure and ceramization kinetics of perhydropolysilazane. *KEM.* 2013, 575–576, 81–6. <https://doi.org/10.4028/www.scientific.net/KEM.575-576.81>
 41. Darken LS, Gurry RW. The system iron-oxygen. I. The wüstite field and related equilibria. *J Am Chem Soc.* 1945, 67(8), 1398–412. <https://doi.org/10.1021/ja01224a050>
 42. Hunt J, Ferrari A, Lita A, Crosswhite M, Ashley B, Stiegman AE. Microwave-specific enhancement of the carbon–carbon dioxide (boudouard) reaction. *J Phys Chem C.* 2013, 117(51), 26871–80. <https://doi.org/10.1021/jp4076965>
 43. Lan R, Irvine JTS, Tao S. Ammonia and related chemicals as potential indirect hydrogen storage materials. *Int J Hydrogen Energy.* 2012, 37(2), 1482–94. <https://doi.org/10.1016/j.ijhydene.2011.10.004>
 44. Liu Y, Wang Y, You Z, Lv X. Reduction and nitridation of iron/vanadium oxides by ammonia gas: mechanism and preparation of FeV45N alloy. *Metals* 2020, 10(3), 356. <https://doi.org/10.3390/met10030356>
 45. Jost W. *Diffusion in solids, liquids, gases (physical chemistry).* 6. New York: Academic Press; 1970.
 46. Tahari ANM, Salleh F, Saharuddin TTS, Samsuri A, Samidin S, Yarmo MA. Influence of hydrogen and carbon monoxide on reduction behavior of iron oxide at high temperature: effect on reduction gas concentrations. *Int J Hydrogen Energy.* 2021, 46(48), 24791–805. <https://doi.org/10.1016/j.ijhydene.2020.06.250>.
 47. Tang MM, Bacon R. Carbonization of cellulose fibers – I. Low temperature pyrolysis. *Carbon* 1964, 2(3), 211–20. [https://doi.org/10.1016/0008-6223\(64\)90035-1](https://doi.org/10.1016/0008-6223(64)90035-1)
 48. Huang X. Fabrication and properties of carbon fibers. *Materials* 2009, 2(4), 2369–403. <https://doi.org/10.3390/ma2042369>
 49. Kim D-Y, Nishiyama Y, Wada M, Kuga S. Graphitization of highly crystalline cellulose. *Carbon* 2001, 39(7), 1051–6. [https://doi.org/10.1016/S0008-6223\(00\)00221-9](https://doi.org/10.1016/S0008-6223(00)00221-9)
 50. Nishimaki K, Ohmae S, Yamamoto TA, Katsura M. Formation of iron-nitrides by the reaction of iron nanoparticles with a stream of ammonia. *Nanostruct Mater.* 1999, 12(1–4), 527–30. [https://doi.org/10.1016/S0965-9773\(99\)00175-0](https://doi.org/10.1016/S0965-9773(99)00175-0)
 51. Wollbrink A, Volgmann K, Koch J, Kanthasamy K, Tegenkamp C, Li Y, et al. Turbostratic and crystalline carbon membranes with hydrogen selectivity. *Carbon* 2016, 106, 93–105. <https://doi.org/10.1016/j.carbon.2016.04.062>
 52. Grainger D, Hägg M-B. Evaluation of cellulose-derived carbon molecular sieve membranes for hydrogen separation from light hydrocarbons. *J Membr Sci.* 2007, 306(1–2), 307–17. <https://doi.org/10.1016/j.memsci.2007.09.005>
 53. Ismail AF, Khulbe KC, Matsuura T. *Gas separation membranes: polymeric and inorganic.* 1st ed. Cham: Springer; 2015. <https://doi.org/10.1007/978-3-319-01095-3>
 54. Kanezashi M, Yamamoto A, Yoshioka T, Tsuru T. Characteristics of ammonia permeation through porous silica membranes. *AIChE J.* 2009;56(5):1204–12. <https://doi.org/10.1002/aic.12059>
 55. Tseng J, Gu D, Pistidda C, Horstmann C, Dornheim M, Ternieden J, et al. Tracking the active catalyst for iron-based ammonia decomposition by in situ synchrotron diffraction studies. *ChemCatChem.* 2018, 10(19), 4465–72. <https://doi.org/10.1002/cctc.201800398>
 56. Eick BM, Youngblood JP. Carbothermal reduction of metal-oxide powders by synthetic pitch to carbide and nitride ceramics. *J Mater Sci.* 2009, 44(5), 1159–71. <https://doi.org/10.1007/s10853-009-3249-6>

How to cite this article: Johannes Peter, Alexander Ott, Ralf Riedel, Emanuel Ionescu, Hans-Joachim Kleebe. Micro-/nanostructure evolution of C/SiFeO(N,C) polymer-derived ceramic papers pyrolyzed in a reactive ammonia atmosphere. *J Am Ceram Soc.* 2022;105:2334–2348. <https://doi.org/10.1111/jace.18237>